Preprint Title	Control over size, shape, and photonics of self-assembled organic nanocrystals
Authors	Chen Shahar, Yaron Tidhar, Yunmin Jung, Haim Weissman, Sidney R. Cohen, Ronit Bitton, Iddo Pinkas, Gilad Haran and Boris Rybtchinski
Publication Date	07 Sep 2020
Article Type	Full Research Paper
Supporting Information File 1	SI _ONCphoto_BJOC.pdf; 1.4 MB
ORCID® iDs	Gilad Haran - https://orcid.org/0000-0003-1837-9779; Boris Rybtchinski - https://orcid.org/0000-0002-2071-8429

Control over size, shape, and photonics of self-assembled organic nanocrystals

Chen Shahar[1], Yaron Tidhar[1], Yunmin Jung[2#], Haim Weissman[1], Sidney R. Cohen[3], Ronit Bitton[4,5], Iddo Pinkas[3], Gilad Haran[2], and Boris Rybtchinski[1]*

Departments of [1]Organic Chemistry, [2]Chemical Physics, and [3]Chemical Research Support, Weizmann Institute of Science, Rehovot 76100, Israel.
[4] Department of Chemical Engineering, and [5]Ilse Katz Institute for Nanoscale science and Nanotechnology Ben-Gurion University, Beer Sheva 84105, Israel.

[#] Current address: Center for Cancer Immunotherapy, La Jolla Institute for Immunology, La Jolla, CA, USA

[*]Corresponding Author

E-mail: boris.rybtchinski@weizmann.ac.il

Abstract

Facile fabrication of free-floating organic nanocrystals (ONCs) was achieved via kinetically controlled self-assembly of simple amphiphilic perylene diimide building blocks in aqueous media. The ONCs have a thin rectangular shape, with the aspect ratio that is controlled via organic co-solvent (THF) content. The nanocrystals were characterized in solution by cryogenic transmission electron microscopy (cryo-TEM) and small angle X-ray scattering (SAXS); the ONCs retain their structure upon drying as was evidenced by TEM and AFM. Photophysical studies, including femtosecond transient absorption spectroscopy, revealed a distinct influence of the ONC morphology on their

photonic properties (excitation energy transfer was observed only in the high aspect ONCs). Convenient control over structure and function of organic nanocrystals can enhance their utility in new and developed technologies.

Keywords: self-assembly; organic nanocrystals; aromatic amphiphiles; exciton diffusion; perylene diimides.

Introduction

Semiconductor and metal nanoparticles exhibit size and morphology-dependent properties arising from confinement effects and strong interactions between neighboring atoms[1–3]. The correlation between nanoparticle size and the related electronic and optical properties was extensively studied, leading to applications in novel technologies and devices[4–6]. The development of the reprecipitation method[7] allowed facile fabrication of (often crystalline) organic nano- and microparticles based on polydiacetylene[8], pyrazoline[9], perylene[10], and other molecules. In several cases, size-dependent absorption was reported[11,12]. These crystals found use in optoelectronic materials[13], as markers for imaging applications[12], and demonstrated anticancer properties[14]. However, control over the size and shape in such systems is challenging[8–16].

Surface chemistry methodologies allow improved control over crystalline product formation; however these methods are indirect and limited by the nature of the interface involved in the process. For example, well-defined two-dimensional nanocrystals were

obtained by the vapor transport method, resulting in improved charge mobility[17], but no control over the crystal size and morphology was demonstrated. Using self-assembled monolayers as templates for the seeding and growth of molecular crystals may offer control over structure and polymorphism[18]. However, in this method, the crystal formation is limited by the monolayer surface, so that it does not allow facile bulk fabrication, and restricts control over the crystal morphology[19,20]. Crystalline nanobelts assembled from perylene and perylene diimide (PDI) derivatives were reported, but their size and shape could not be controlled[21,22]. Modification of the building blocks in such systems result in a certain degree of control[23,24], yet the PDI nanobelts do not remain free-floating in solution and normally are characterized as solid state materials[25], limiting the processability of the nanocrystals, control over their morphology, and insights into their assembly.

In general, gaining control over crystal formation represents a long-standing challenge[26–28]. In this respect, understanding and controlling the crystallization process is key to fabricating organic nanocrystals with predesigned morphology and properties[29]. We have reported on 2D crystalline self-assembled systems based on a hierarchical assembly mode promoted by hydrophobic and π-π interactions[30]. Yet, the size and shape of these systems could not be controlled beyond the 2D morphology.

We report herein on aqueous self-assembly of organic nanocrystals with tunable aspect ratio. These systems are quite uniform and exhibit morphology-dependent photonics: strikingly divergent exciton diffusion properties as a function of their shape.

Results and discussion

Following our interest in self-assembly of amphiphilic perylene diimide (PDI) derivatives, we employed compound **1**, a PDI system with a hydrophilic group (phenoxy benzoic acid) attached to the aromatic core of PDI at the bay area [29c]. Compound **1** is an asymmetric amphiphile that was designed to result in arrays that differ from fibrous and monolayer structures assembled from symmetrically substituted bolaamphiphilic PDI systems[30,31].

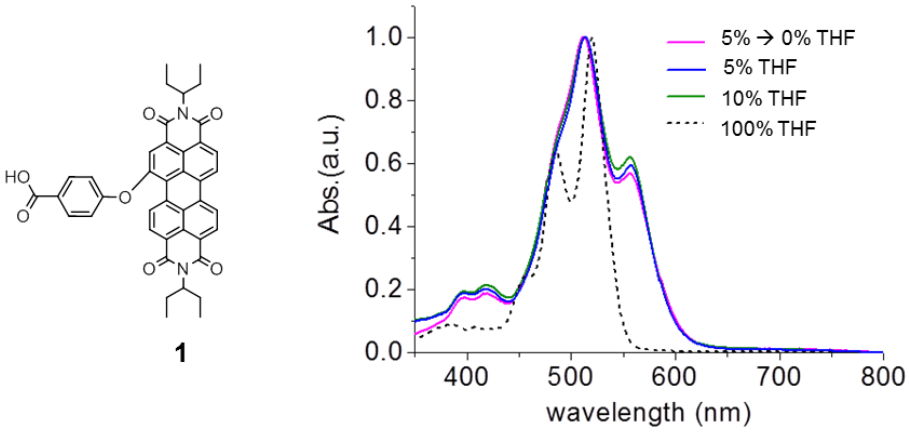

Figure 1: Chemical structure of compound **1** and UV-vis spectra in aggregating aqueous media and in disaggregating solvent (THF).

Crystalline Self-Assembly. We have found that noncalssical crystallization of **1** in neutral aqueous solutions can be manipulated to result in different polymorphs[29c], 3D crystals with dissimilar structures and morphologies. We envisaged that crystallization of **1** in basic aqueous media can lead to 2D arrays (bilayers) due to the higher solubility of the

assemblies as a result of charged carboxylate groups that are expected to favor solvation by water. We induced the self-assembly process by injecting concentrated solution of **1** in THF (2×10^{-3} M) into basic water (pH 10), or a water/THF mixture to reach 1×10^{-4} M concentration. We studied the following three assembly conditions: **10% THF**, injection of the stock solution to basic water/THF mixture to obtain 10% THF content by volume; **5% THF**, injection of the stock solution to basic water to give 5% THF content; **5% → 0% THF**, injection of the stock solution to basic water to result in 5% THF content, followed by the immediate evaporation of THF under high vacuum and adding water to reach 1×10^{-4} M concentration.

The self-assembly is instantaneous as indicated by a color change from bright orange to pink in all systems. UV-vis spectra of compound **1** in aqueous medium exhibit 0-0/0-1 vibronic band inversion, red shift and significant broadening in comparison with the molecularly dissolved system (Figure 1B). This is a typical spectral signature of ordered PDI systems and crystals[32–36] having face-to-face orientation of π-systems.

Cryo-TEM and TEM studies reveal that the **10% THF** assemblies are long rectangular-shaped crystals, ~3 μm in length (Figures 2A). The crystals have an aspect ratio of 2.6±1.3 and their crystalline order was evident from Fast Fourier Transform (FFT) analysis, exhibiting well-defined spots corresponding to periodicity of 1.6 nm. **5% THF** assembly gave rise to crystals that are ~1 μm in length, with an aspect ratio of 5.0±1.9. FFT analysis revealed the spacing value of 1.6 nm, identical to **10% THF** system (Figure 2B). In the case of **5% → 0% THF**, the crystals were over 5 μm long and under 0.5 μm in width, thus having the largest aspect ratio amongst the studied systems: 10±3.5. Crystalline order gave rise to 1.6 nm spacing as indicated by FFT (Figures 2C). The

aspect ratio values and the calculated standard deviations are based on two different assembly solutions including 50 crystals for each system.

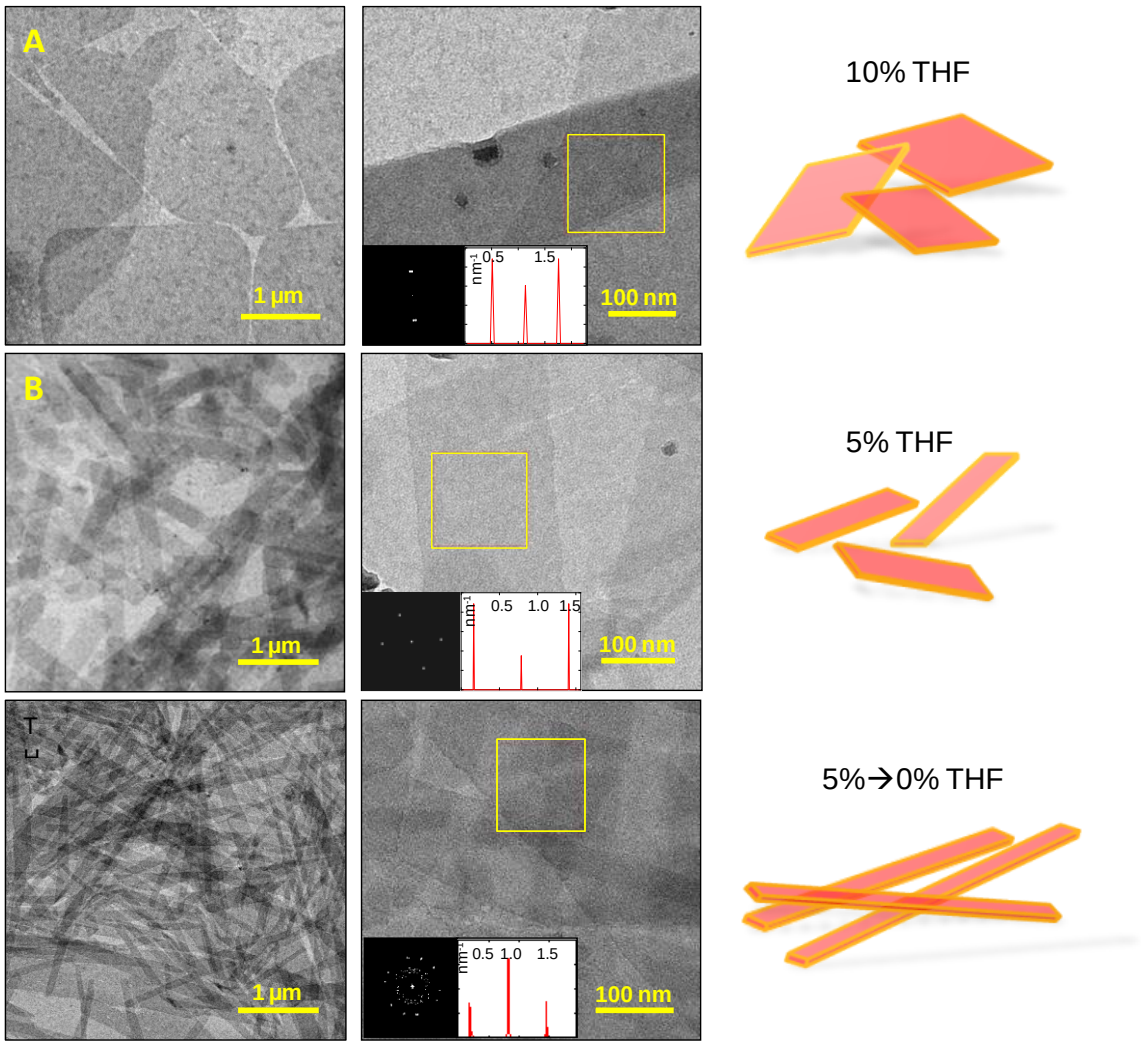

Figure 2: TEM images (left, zoomed-out and zoomed-in; 1×10^{-4} M solutions of **1** deposited on TEM grids) and crystal morphology sketches (right):. A) **10% THF**. B) **5% THF**. C) **5%→0%THF**. Insets: FFT analysis of the crystalline material (in the marked areas), demonstrating identical spacing of 1.6 nm in all systems.

All obtained crystalline assemblies demonstrated structural stability toward drying and presented an identical fine structure composed of an ordered array of alternating dark and light contrast stripes as observed by TEM and cryo-TEM (Figures 2 and 3 respectively).

FFT indicates crystallinity (well defined spots) and identical spacings in all systems. Image analysis revealed 0.96±0.10 nm dark-contrast stripes separated by 0.69±0.12 nm light-contrast stripes in all cases. The molecular model that best fits the cryo-TEM and TEM data is a bilayer, where pairs of PDI cores are coupled together and the carboxylic groups of both PDIs turn outwards to the surrounding aqueous media. The resulting 1D π-stacked bi-layer structures interact via the ethyl propyl residues to form an extended bi-layered crystalline sheet (Figure 3E). According to the model (Figure 3C), dark contrast stripes correspond to the overlapping aromatic cores (1.1 nm), and the light contrast stripes correspond to the ethyl propyl residues (0.6 nm) as observed in cryo-TEM images (Figure 3A, B).

In order to validate the bilayer width of the nanocrystals, atomic force microscopy (AFM) and small angle X-ray scattering (SAXS) measurements of the assembled compound **1** were employed. An air-dried sample of compound **1** deposited on a Si substrate (See Supporting Information for details) gave rise to rectangular structures with well-defined edges (Figure S3), 3.2±0.4 nm in height. This is in good agreement with the bilayer width in the molecular model, corresponding to the oxygen-oxygen distance between the carboxylic groups of two adjacent PDIs (Figure S2 B,C). Small angle X-ray scattering (6×10^{-4} M aqueous solution of **1**, 5% THF, Figure S4) demonstrated a power-law dependence of q^{-2} in the low q region, indicative of flat particles[37]. The background subtracted curve could be fit to a dilute lamellar form factor (equation 3 in Supporting Information) to give an overall thickness of 35±3Å, which is in excellent agreement with the molecular modeling and the AFM results.

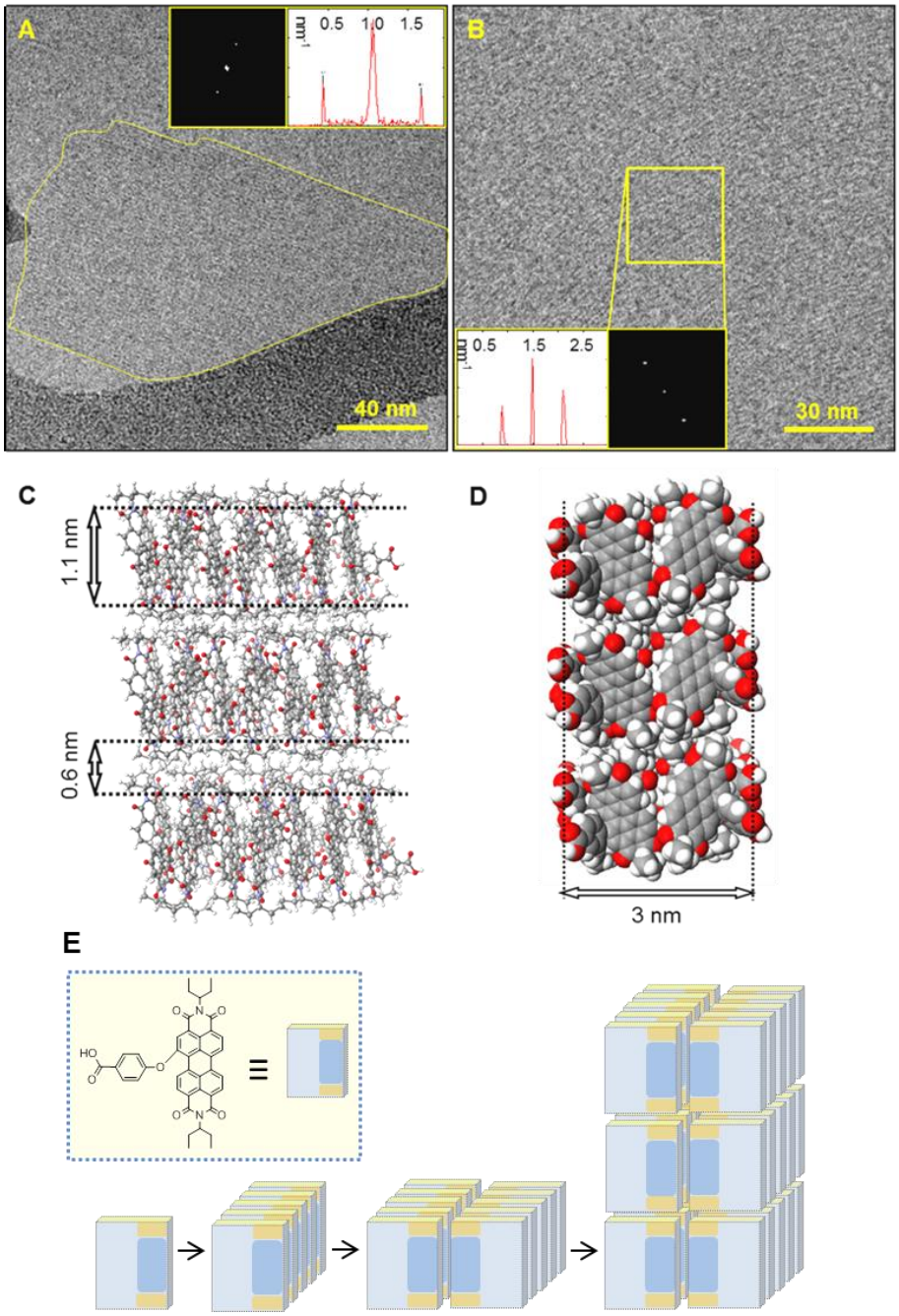

Figure 3: Cryo-TEM images of 1×10^{-4} M solution of **1** (5% THF) and the corresponding molecular model and a cartoon illustrating the self-assembly process. A) cryo-TEM image, the crystal is highlighted with a yellow contour. B) Zoom-in showing fine-structure composed of alternating dark and light contrast stripes. Insets: FFT analysis of the crystalline material giving rise to a spacing value of 1.6 nm. (C-D) Molecular model: C) the interacting stacks and their dimensions corresponding to the observed fine-structure; D) cross-section demonstrating the

bilayer structure composed of two adjacent PDI cores. The measured distance (3 nm) corresponds to the oxygen-oxygen distance between the carboxylic groups of two PDIs. E) Schematic representation of the assembly structuring.

The presented crystalline structures are kinetically trapped products since they do not equilibrate upon changing the assembly conditions after they are fully formed. Thus, addition of THF to pre-assembled **5%→0% THF** crystals to 5% THF content did not result in any observable morphological change (Figure S6B). Similarly, when THF was added to the assembled **5% THF** material to result in 10% THF content (Figure S6A) no change was observed. Evidently, the structure of the crystals is defined by the assembly pathway rather than equilibration at a given solvent composition.

In order to gain insight into the crystallization mechanism and the effect of the THF concentration on the crystallization process, we performed cryo-TEM imaging of the early assembly stages. In the case of **5% THF**, monomolecular 1D stacks, 1.5±0.3 nm in width were observed after 1 min aging (Figure 4A). The assembled material appeared as short fibers (10-80 nm length), some of which interact and align. In the case of **10% THF**, crystalline arrays ~100 nm in length and ~10 nm in width were observed after 1 min (Figure 4B). The structural differences between **5% THF** and **10% THF** systems at early assembly times reveal the distinct dynamics of the nucleation/growth process. Thus, the **10% THF** system shows a faster ordering process (THF makes the system more dynamic, lowering activation barriers for molecular reorganization[38]), resulting in long rigid fibers that interact (Figure 3E), leading to larger ordered arrays and templating the further assembly process. This, together with better stabilization of the aromatic cores at higher THF content, leads to large, low aspect ratio crystals in **10% THF** case. Thus,

kinetically controlled pathway-dependent nucleation/growth defines the outcome of the crystalline self-assembly process. In both **5% THF** and **10% THF** systems, the crystallization is largely completed after 5 min (Figure S7). The observed crystallization pathways are consistent with gradual order evolution mechanisms recently observed by us[29b].

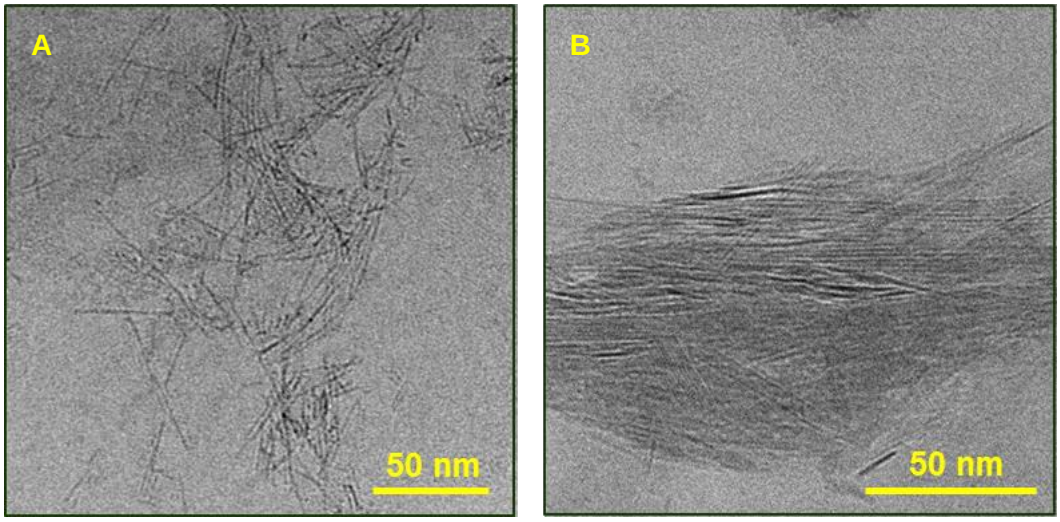

Figure 4: Cryo-TEM images of 1×10^{-4} M compound **1** in THF/water solutions after one minute of aging. A) 5% THF: monomolecular 1D π-stack fibers B) 10% THF: crystalline platelets.

Controlling the crystal morphology also can be achieved in an alternative fashion using variation in pH (Figure S8). However, crystals assembled under different pH conditions are less homogeneous and demonstrate a larger size distribution than the crystals obtained using control via THF content.

Exciton dynamics. In order to investigate whether the morphology affects photonic properties, we studied the excited state dynamics of the nanocrystals. Femtosecond

transient absorption (fsTA) spectra of all assemblies displayed typical PDI excited state absorption peaks in the range of 600-770 nm[39], matching PDI bleaching represented by negative features at 550-600 nm. In the disaggregated state, almost no power dependence was observed. The decay kinetics of **5% THF** and **5%→0% THF** systems demonstrated power dependence (Figure 5A and S9A respectively). In contrast, **10% THF** nanocrystals exhibit essentially *power-independent* kinetics (Figure 5B). Power dependence is indicative of the exciton-exciton annihilation process, occurring when a high photon flux results in multiple excitons which can efficiently diffuse through the aggregated material resulting in exciton annihilation.[40]

In order to validate the observed behavior and prove that the measured differences between **5% THF** and **10% THF** assemblies stem from the different crystal morphology and not from the difference in THF concentration, a control experiment was performed. A sample of **1** prepared in **5% THF** was aged for two days, after which the THF concentration was adjusted to 10%. The control sample was measured, showing exciton dynamics very similar to the original **5% THF** sample (Table 1, Figure S9B).

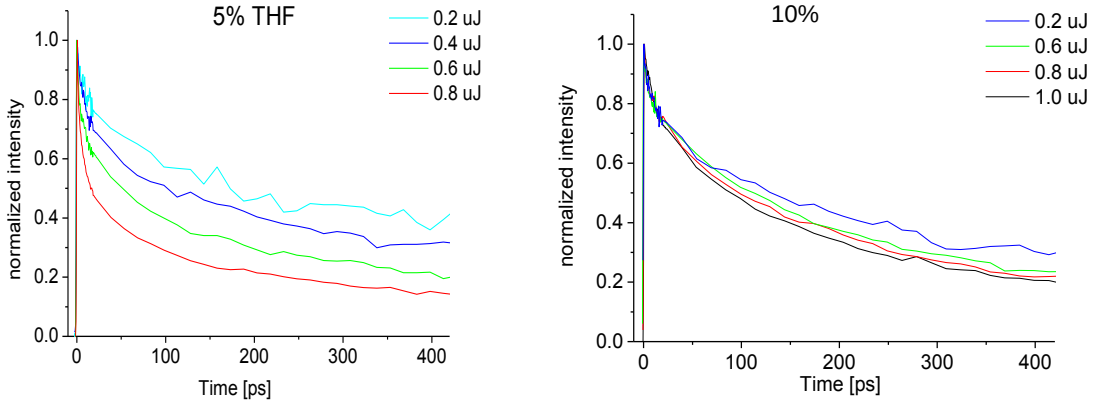

Figure 5: Transient kinetics at different laser powers probed at 755 nm (1×10^{-4} M solution at pH10): A) 5% THF solution. B) 10% THF solution.

In order to estimate exciton diffusion coefficient and diffusion length we used an analysis method employed in our previous work,[30] and based on a one-dimensional diffusion model for the annihilation rate[41–44]. The model fits our data, revealing that exciton diffusion occurs primarily within 1D aromatic stacks, in agreement with the reported annihilation studies[43,44]. The fitted data is presented in Figures S10-S12 and the exciton diffusion parameters are given in Table 1:

Table 1. Diffusion coefficient and exciton diffusion length

Measured crystal system	***D*, cm²/s**	**L_D^*, nm**
5% → 0% THF	0.07±0.01	198±4
5% THF	0.05±0.01	170±13
pre-aged **5% THF** adjusted to **10% THF**	0.04±0.01	114±14
10% THF	No power dependence	

*Exciton diffusion length is calculated using $L_D = \sqrt{D\tau}$, where τ is the exciton lifetime (estimated as a longer decay component of the decay fit, representing a lower limit for the exciton lifetime).

5% THF and **5%→0% THF** systems gave rise to similar diffusion coefficients: 5×10^{-2} cm^2/s and 7×10^{-2} cm^2/s respectively. These values are comparable with the reported exciton diffusion coefficients of 2D PDI crystalline arrays reported by us[25] and those of PTCDA (perylene tetracarboxylic dianhydride) solid crystalline films (4×10^{-2} cm^2/s)[41]. Exciton diffusion lengths in the assembled material are also comparable or higher than the reported values for 2D PDI crystals (120 nm)[25], PTCDA films (61 nm)[41] and PDI J-aggregates (96 nm)[45], indicating efficient exciton hopping. **10% THF** assembly showed almost no power dependence, in striking difference to other systems. This can be attributed to the exciton trapping[21], probably at the large aromatic "edges" in the **10% THF** crystals.

Super-resolution fluorescence microscopy measurements were carried out in order to further study the photonic behavior of the systems. Interestingly, the **5% THF** system displayed emission that was localized at regions that appeared to be matching the shape and dimensions of the crystal's edges (Figure S13), with a clear preference for emission at the crystal corners (the microscopy of the **10% THF** system did not provide reliable super-resolution images). This further underscores the influence of crystal morphology on the photonic properties,[46] and will be a subject of future studies.

Experimental

General information. The ^{1}H, and ^{13}C NMR spectra were recorded at 20 °C on 300 MHz NMR spectrometer (Bruker). Electrospray Ionization (ESI) Mass-Spectrometry was performed using Micromass Platform instrument. UV-vis absorption and fluorescence

measurements were carried out on a Cary-5000 spectrometer (Varian) and Cary Eclipse fluorimeter (Varian), respectively.

Preparation of assemblies Samples of compound **1** were prepared by dissolving the dry material in THF followed by the injection of the THF solution into double-distilled water (Barnstead NANOpure Diamond water system, used for all sample preparations) at the desired pH (adjusted by adding NaOH solution). 5%→0% THF samples were prepared by an immediate evaporation of the THF co-solvent, followed by dilution with water to the desired final concentration. Clear homogeneous pink solutions were obtained.

Transmission electron microscopy (TEM) imaging was performed using Tecnai T12 transmission electron microscope operated at 120 kV. *Sample-preparation:* 8 µl of each sample was applied to a 400-mesh copper grid coated with carbon (on nitrocellulose support) and blotted 2 minutes later from the back side of the grid.

Cryo-transmission electron microscopy (cryo-TEM) imaging was performed using a Tecnai F20 transmission electron microscope operating at 200 kV, and using a Gatan 626 cooling holder and transfer station with a Gatan US4000 CCD digital camera, or a Tecnai T12 transmission electron microscope operated at 120 kV, using a Gatan 626 cooling holder and transfer station, with a TVIPS F244HD CCD digital camera. *Sample-preparation:* 8 µL of each sample was applied to a 300-mesh copper grid coated with holey carbon (Pacific Grid-Tech supplies). The samples were blotted at 25°C and 95% relative humidity, and plunged into liquid ethane using Leica EM-GP Automatic Grid Plunger. Specimens were equilibrated at -178°C in the microscope prior to the imaging process. Time dependent cryo-TEM samples were prepared just before the plunging,

using a stopwatch. The same assembly solution that was plunged at t=1 minute was used again at t=5 minutes and t=30 minutes in order to elucidate the structural evolution of the self-assembled crystals.

Femtosecond transient absorption spectroscopy was performed using a system based on a mode-locked Ti:sapphire oscillator (Spectra Physics MaiTai). The oscillator produces a train of <120-fs pulses (bandwidth ~10 nm FWHM), with a peak wavelength centered at 800 nm. The weak oscillator pulses are amplified by a chirped pulse regenerative amplifier (CPA) (Spectra Physics Spitfire ACE). The pulses are first stretched, then regeneratively amplified in a Ti:sapphire cavity, pumped by a pulsed Nd :YLF laser (Spectra Physics Empower 45) operating at 1 kHz. After the pulse has been amplified and recompressed, its energy is about 5.0 mJ in a train of 1-kHz pulses, and about 1mJ is used in the transient absorption set-up. An independent pump pulse is obtained by pumping an optical parametric amplifier (Spectra Physics OPA-800CF) that produces 120-fs pulses tunable from 300 nm to 3 μm. The output power of the OPA is a few micro joules (depending on the chosen wavelength) at 1 kHz. The pump beam is mechanically chopped at half the amplifier repetition rate. The chopper (C-995 TTI) is synchronized with the Spitfire pulses. Normally a few thousand pulse pairs (pump on/pump off) are averaged to produce a transient absorption spectrum with a noise level below 0.3 mOD. A small portion of the remaining amplified pulse is used to generate a white light continuum as a probe pulse. To this end, the Ti:sapphire beam is focused onto a 3-mm thick sapphire disk by a 10-cm focal length lens, and the numerical aperture of the beam is controlled by an iris placed in front of the lens to obtain a stable and smooth white light continuum. The resulting beam is passed through a Raman notch filter in order to remove

the remains of the 800 nm fundamental beam from the probe white light continuum. The pump and probe pulses are crossed in the sample at a small angle, while maintaining a magic angle between the pump and probe polarizations. The remains of the pump pulse are removed by passing the probe through an iris, and it is then imaged onto an optical fiber that brings it into a fiber optic interface, which focuses the light onto the entrance slit of a Jobin Yivon Triax 180 spectrograph. The light is normally dispersed by a 300 gr/mm grating onto a fast CCD camera (Andor Newton DU-970N-UV, operating at 1,000 spectra per second using "crop mode"). The whole setup is controlled by National Instruments LabView software. A variable neutral-density filter was employed to adjust the pump power for studying the power dependence. The pump power intensities were measured using an Ophir powermeter with a photodiode sensor in proximity to the sample. The excitation densities were calculated for a laser spot of 300 μm diameter on the sample. This diameter was measured by placing beamprofiler (Ophir Beamstar FX33) at the sample position and determining the 4-sigma (95% of the power) parameter. In the reported experiments the pump was tuned to 525 or to 590 nm and the optical densities of the samples (in 4 mm and 2 mm optical path length cuvettes) were kept between 0.2 and 0.5 at the excitation wavelength. The instrument response function (300 fs) was recorded by repetition of the experiments with sample replaced by pure solvent and keeping all other parameters unchanged. Spectral corrections and analysis were performed using Surface Xplorer Pro (Ultrafast Systems) and Origin 7.5 (OriginLab) software.

Conclusions

We have demonstrated that a simple amphiphilic building block assembles into well-defined free-floating crystals in aqueous media. The crystalline assemblies are stable and their morphology can be fine-tuned as a function of the initial THF concentration or the pH in the assembly solution. The nanocrystals demonstrate morphologically-dependent photonic properties, showing uniquely dissimilar exciton diffusion behavior. Facile fabrication of well-defined nanocrystals combined with the ability to control their morphology and photonic properties represents a convenient structure/function tool advancing the applicability of organic nanocrystals.

Supporting Information

Supporting Information File 1.

Funding

This work was supported by grants from the Israel Science Foundation, Minerva Foundation, Schmidt Minerva Center for Supramolecular Architectures, and the Helen and Martin Kimmel Center for Molecular Design.

References

1. Brus, L. *Appl. Phys. A* **1991**, *53*, 465–474.

2. Kelly, K. L.; Coronado, E.; Zhao, L. L.; Schatz, G. C. *J. Phys. Chem. B* **2003**, *107*, 668–677.

3. Alivisatos, A. P. *Science* **1996**, *271*, 933–937.

4. Halperin, W. *Rev. Mod. Phys.* **1986**, *58*, 533–606.

5. Peng, X.; Schlamp, M. C.; Kadavanich, A. V.; Alivisatos, A. P. *J. Am. Chem. Soc.* **1997**, *119*, 7019–7029.

6. Colvin, V. L.; Schlamp, M. C.; Alivisatos, A. P. *Nature* **1994**, *370*, 354–357.

7. Kasai, H.; Nalwa, H. S.; Oikawa, H.; Okada, S.; Matsuda, H.; Minami, N.; Kakuta, A.; Ono, K.; Mukoh, A.; Nakanishi, H. *Jpn. J. Appl. Phys.* **1992**, *31*, L1132–L1134.

8. Iida, R.; Kamatani, H.; Kasai, H.; Okada, S.; Oikawa, H.; Matsuda, H.; Kakuta, A.; Nakanishi, H. *Mol. Cryst. Liq. Cryst. Sci. Technol. A.* **1995**, *267*, 95–100.

9. Fu, H.-B.; Wang, Y.-Q.; Yao, J.-N. *Chem. Phys. Lett.* **2000**, 322, 327–332.

10. Kasai, H.; Kamatani, H.; Okada, S.; Oikawa, H.; Matsuda, H.; Nakanishi, H. *Jpn. J. Appl. Phys.* **1996**, *35*, L221–L223.

11. Fu, H.-B.; Yao, J.-N. *J. Am. Chem. Soc.* **2001**, *123*, 1434–1439.

12. (a) Baba, K.; Kasai, H.; Masuhara, A.; Oikawa, H.; Nakanishi, H. *Jpn. J. Appl. Phys.* **2009**, *48*, 117002–2 –117002–4. (b) Fery-Forgues, S. *Nanoscale* **2013**, *5*, 8428-8442.

13. (a) Nakanishi H.; Katagi, H. *Supramol. Sci.* **1998**, *5*, 289–295. (b) Rosenne, S.; Grinvald, E.; Shirman, E.; Neeman, L.; Dutta, S.; Bar-Elli, O.; Ben-Zvi, R.; Oksenberg, E.; Milko, P.; Kalchenko, V.; Weissman, H.; Oron, D.; Rybtchinski, B. *Nano Lett.* **2015**, *15*, 7232-7237. (c) Schierl, C.; Niazov-Elkan, A.; Shimon, L. J. W.; Feldman, Y.; Rybtchinski, B.; Guldi, D. M. *Nanoscale* **2018**, *10*, 20147-20154.

14. Kasai, H.; Murakami, T.; Ikuta, Y.; Koseki, Y.; Baba, K.; Oikawa, H.; Nakanishi, H.; Okada, M.; Shoji, M.; Ueda, M.; Imahori, H.; Hashida, M. *Angew. Chem. Int. Ed.* **2012**, *51*, 10315–10318.

15. Zhao, Y. S.; Fu, H.; Peng, A.; Ma, Y.; Xiao, D.; Yao, J. *Adv. Mater.* **2008**, *20*, 2859–2876.

16. Komai, Y.; Kasai, H.; Hirakoso, H.; Hakuta, Y.; Okada, S.; Oikawa, H.; Adschiri, T.; Inomata, H.; Arai, K.; Nakanishi, H. *Mol. Cryst. Liq. Cryst. Sci. Technol. A.* **1998**, *322*, 167–172.

17. Jiang, H.; Zhang, K. K.; Ye, J.; Wei, F.; Hu, P.; Guo, J.; Liang, C.; Chen, X.; Zhao, Y.; McNeil, L. E.; Hu, W.; Kloc, C. *Small* **2013**, *9*, 990–995.

18. Hiremath, R.; Basile, J. A.; Varney, S. W.; Swift, J. A. *J. Am. Chem. Soc.* **2005**, *127*, 18321–18327.

19. Kang, J. F.; Zaccaro, J.; Ulman, A.; Myerson, A. *Langmuir* **2000**, *16*, 3791–3796.

20. Briseno, A. L.; Aizenberg, J.; Han, Y.; Penkala, R. A.; Moon, H.; Lovinger, A. J.; Kloc, C.; Bao, Z. *J. Am. Chem. Soc.* **2005**, *127*, 12164–12165.

21. Kim, B. J.; Yu, H.; Oh, J. H.; Kang, M. S.; Cho, J. H. *J. Phys. Chem. C* **2013**, *117*, 10743–10749.

22. Balakrishnan, K.; Datar, A.; Oitker, R.; Chen, H.; Zuo, J.; Zang, L. *J. Am. Chem. Soc.* **2005**, *127*, 10496–10497.

23. Balakrishnan, K.; Datar, A.; Naddo, T.; Huang, J.; Oitker, R.; Yen, M.; Zhao, J., Zang, L. *J. Am. Chem. Soc.* **2006**, *128*, 7390–7398.

24. Zhang, Z.; Zhang, X.; Zhan, C.; Lu, Z.; Ding, X.; He, S.; Yao, J. *Soft Matter* **2013**, *9*, 3089–3097.

25. Che, Y.; Datar, A.; Balakrishnan, K.; Zang, L. *J. Am. Chem. Soc.* **2007**, *129*, 7234–7235.

26. Weissbuch, I.; Lahav, M.; Leiserowitz, L. *Cryst. Growth Des.* **2003**, *3*, 125–150.

27. (a) Vekilov, P. G. *Cryst. Growth Des.* **2010**, *10*, 5007–5019. (b) Jehannin, M.; Rao, A.; Colfen, H. *J. Am. Chem. Soc.* **2019**, *141*, 10120-10136.

28. Sear, R. P. *Int. Mater. Rev.* **2012**, *57*, 328–356.

29. (a) Davey, R. J.; Schroeder, S. L. M.; Ter Horst, J. H. *Angew. Chem. Int. Ed.* **2013**, *52*, 2166–2179. (b) Tsarfati, Y.; Rosenne, S.; Weissman, H.; Shimon, L. J. W.; Gur, D.; Palmer, B. A.; Rybtchinski, B. *ACS Cent. Sci.* **2018**, *4*, 1031-1036. (c) Shahar, C.; Dutta, S.; Weissman, H.; Shimon, L. J. W.; Ott, H.; Rybtchinski, B. *Angew. Chem. Int. Ed.* **2016**, *55*, 179-182.

30. Shahar, C.; Baram, J.; Tidhar, Y.; Weissman, H.; Cohen, S. R.; Pinkas, I., Rybtchinski, B. *ACS Nano* **2013**, *7*, 3547–3556.

31. (a) Krieg, E.; Rybtchinski, B. *Chem. Eur. J.* **2011**, *17*, 9016–9026. (b) Krieg, E.; Niazov-Elkan, A.; Cohen, E.; Tsarfati, Y.; Rybtchinski, B. Noncovalent Aqua Materials Based on Perylene Diimides. *Acc. Chem. Res.* **2019**, *52*, 2634-2646.

32. Cormier, R. A.; Gregg, B. A. *Chem. Mater.* **1998**, *10*, 1309–1319.

33. Kazmaier, P. M.; Hoffmann, R. *J. Am. Chem. Soc.* **1994**, *116*, 9684–9691.

34. Klebe, G.; Graser, F.; Hädicke, E.; Berndt, J. *Acta Crystallogr. B* **1989**, *45*, 69–77.

35. Zang, L.; Che, Y.; Moore, J. S. *Acc. Chem. Res.* **2008**, *41*, 1596–608.

36. Würthner, F.; Bauer, C.; Stepanenko, V.; Yagai, S. *Adv. Mater.* **2008**, *20*, 1695–1698.

37. Glatter, O.; Kratky, O. *Small Angle X-ray Scattering*, Academic Press, London, 1982.

38. Tidhar, Y.; Weissman, H.; Wolf, S. G.; Gulino, A.; Rybtchinski, B. *Chem. Eur. J.* **2011**, *17*, 6068–6075.

39. Wasielewski, M. R. *J. Org. Chem.* **2006**, *71*, 5051–5066.

40. Pope, C. E.; Swenberg, M. *Electronic Processes in Organic Crystals and Polymers*, Oxford University Press, 1999.

41. Engel, E.; Leo, K.; Hoffmann, M. *Chem. Phys.* **2006**, *325*, 170–177.

42. Ahrens, M. J.; Sinks, L. E.; Rybtchinski, B.; Liu, W.; Jones, B.; Giaimo, J. M.; Gusev, A. V.; Goshe, A. J.; Tiede, D. M.; Wasielewski, M. R. *J. Am. Chem. Soc.* **2004**, *126*, 8284–94.

43. Suna, A. *Phys. Rev. B* **1970**, *1*, 1716–1739.

44. Inoue, A.; Yoshihara, K.; Nagakura, S. *Bull. Chem. Soc. Jpn.* **1972**, *45*, 1973–1976.

45. Marciniak, H.; Li, X.-Q.; Würthner, F.; Lochbrunner, S. *J. Phys. Chem. A* **2011**, *115*, 648–654.

46. Bisri, S. Z.; Takenobu, T.; Yomogida, Y.; Shimotani, H.; Yamao, T.; Hotta, S.; Iwasa, Y. *Adv. Funct. Mater.* **2009**, *19*, 1728–1735.